30.3 A Bias-Flip Rectifier with a Duty-Cycle-Based MPPT Algorithm for Piezoelectric Energy Harvesting with 98% Peak MPPT Efficiency and 738% Energy-Extraction Enhancement

Yue, Xinling; Javvaji, Sundeep; Tang, Zhong; Makinwa, Kofi A.A.; Du, Sijun

DOI
10.1109/ISSCC42615.2023.10067284

Publication date
2023

Document Version
Final published version

Published in
2023 IEEE International Solid-State Circuits Conference, ISSCC 2023

Citation (APA)
Yue, X., Javvaji, S., Tang, Z., Makinwa, K. A. A., & Du, S. (2023). 30.3 A Bias-Flip Rectifier with a Duty-Cycle-Based MPPT Algorithm for Piezoelectric Energy Harvesting with 98% Peak MPPT Efficiency and 738% Energy-Extraction Enhancement. In *2023 IEEE International Solid-State Circuits Conference, ISSCC 2023* (pp. 442-444). (Digest of Technical Papers - IEEE International Solid-State Circuits Conference; Vol. 2023-February). IEEE. https://doi.org/10.1109/ISSCC42615.2023.10067284

30.3 A Bias-Flip Rectifier with a Duty-Cycle-Based MPPT Algorithm for Piezoelectric Energy Harvesting with 98% Peak MPPT Efficiency and 738% Energy-Extraction Enhancement

Xinling Yue, Sundeep Javvaji, Zhong Tang, Kofi A.A. Makinwa, Sijun Du

Delft University of Technology, Delft, The Netherlands

Synchronized bias-flip rectifiers, such as synchronized switch harvesting on inductor (SSHI) rectifiers, are widely used for piezoelectric energy harvesting (PEH) [1], which can replace the use of batteries in many IoT applications, thus reducing both system volume and maintenance cost. However, the output power extracted by such rectifiers strongly depends on the impedance matching between the piezoelectric transducer (PT) and the circuit. To maximize this, two maximum power point tracking (MPPT) algorithms are often used. As shown in Fig. 30.3.1 (left), the Perturb & Observe (P&O) (a.k.a. hill-climbing) algorithm adjusts the rectified output power in a stepwise manner towards the maximum power point (MPP), thus establishing robust and continuous MPPT. However, accurately sensing the rectified output power often requires complex and power-hungry hardware [1, 2]. Another simpler algorithm is based on the fractional open-circuit voltage (FOCV) and involves periodically measuring the PT's open-circuit voltage amplitude (V_{OC}) and regulating the rectified voltage (V_{REC}) to a level (V_{MPP}), which corresponds to the MPP [3–6]. However, the PT must be periodically disconnected from the rectifier to measure V_{OC}, resulting in wasted energy, while the inherent delay in sensing V_{OC} variations reduces the overall tracking efficiency. Furthermore, a calibration step is usually necessary to determine V_{MPP}, since this depends on the actual PT voltage flip efficiency (η_F) of the bias-flip rectifier.

In this paper, a duty-cycle-based MPPT algorithm is proposed, which combines the advantages of the P&O and FOCV algorithms while eliminating their drawbacks. As shown in Fig. 30.3.1 (right), when a weakly coupled PT is vibrating at its natural frequency, it can be modelled as an AC current source I_P in parallel with a capacitor C_P. The system consists of an SSHI rectifier, a buck-boost DC-DC converter to adjust the V_{REC}, and an MPPT controller. While extracting the AC energy from the PT, the rectifier switches periodically between conducting and cut-off modes. It generates a cut-off signal, *CO*, which is "high" when the rectifier is cut-off and "low" when it is conducting (the red waveform). The proposed MPPT algorithm exploits the relationship between the MPPT efficiency (η_{MPPT}) and the duty-cycle of *CO* (D_{CO}). Through mathematical analysis, this work finds that $\eta_{MPPT}=1-\cos^2(\pi D_{CO})$, where η_{MPPT} is the ratio of the actual rectified power to the optimal output power at the MPP. As shown in Fig. 30.3.1 (right), operation at the MPP can then be achieved by regulating D_{CO} to 50%, regardless of V_{OC} and η_F. Furthermore, due to the squared cosine relationship, the algorithm is robust to D_{CO} sensing errors. For example, a D_{CO} error of ±5% (or ±10%) results in η_{MPPT} still greater than 97% (or 90%). Compared to the conventional P&O and FOCV, the proposed duty-cycle-based MPPT algorithm has the following advantages: 1) it is independent of V_{OC} or η_F, so no calibration is required; 2) the PT is always connected to the rectifier, so no energy is wasted; and 3) continuous MPPT is possible. These advantages simplify its circuit implementation, resulting in a prototype PEH dissipating only 307nW in the MPPT controller.

The flowchart of the proposed MPPT algorithm is shown in Fig. 30.3.2 (top). The D_{CO}, is sampled in every *CO* period by measuring its ON and OFF pulse widths. If $D_{CO}<50\%$, energy harvested by the PT will charge the rectifier output capacitor C_{REC}, thus increasing its voltage V_{REC} towards the MPP. If D_{CO} exceeds 50%, this means that V_{REC} exceeds the V_{MPP}, so some of the energy in C_{REC} is transferred to the storage capacitor C_S via a DC-DC buck-boost converter in order to maintain V_{REC} around V_{MPP} by regulating D_{CO} to around 50%. At the beginning of the DC-DC transfer, a voltage level V_{RECS}, which is slightly lower than the initial V_{REC}, is set as the lower threshold of the V_{REC} hysteresis window. Clocked by an on-chip oscillator (OSC), the buck-boost conversion operates for multiple cycles until $V_{REC}<V_{RECS}$. This flow will repeat until next time when D_{CO} exceeds 50%, to achieve MPPT.

The proposed architecture consists of an SSHI rectifier with its own control block, and a buck-boost converter with an MPPT controller (Fig. 30.3.2). The SSHI rectifier consists of an FBR, an active diode and an off-chip inductor L_M shared with the DC-DC converter. When the voltage across the PT (V_{PT}) needs to be flipped, the FBR switches from conducting mode to cut-off mode. This causes a *CO* rising edge, which is used to generate an SSHI flipping pulse that briefly connects L_M across the PT, thus initiating a closed RLC loop to flip V_{PT}. The *CO* signal is also sent to the MPPT controller, where its duty-cycle D_{CO} is measured. If D_{CO} exceeds 50%, the DC-DC converter is enabled at the next low-*CO* period to transfer some energy from C_{REC} to C_S, and thus maintaining V_{REC} around the V_{MPP}. A hysteresis window, with a lower threshold V_{RECS} (a fraction of the initial V_{REC}), prevents V_{REC} from dropping too much. The upper hysteresis threshold is automatically set to V_{MPP} by the D_{CO}=50% condition, and so an explicit voltage threshold is not required. The buck-boost converter is controlled by an on-chip OSC, and uses the shared L_M to transfer energy from C_{REC} to C_S. The timing of the switching signal, S_{PD}, is controlled by a zero-crossing detector (ZCD).

Figure 30.3.3 shows the MPPT controller. The D_{CO} is sensed by two equal on-chip capacitors, C_{RGL} and C_{RGR}. When *CO* is high, C_{RGL} is charged by an on-chip current source to V_H; while C_{RGR} is charged to V_L when *CO* is low. To cope with a wide range of PT vibration frequency (half of *CO* frequency), C_{RGL} and C_{RGR} can be adjusted in 8 steps between 5.4pF and 32.2pF. The resulting voltages V_H and V_L are compared to generate the *PO* signal, which indicates the polarity of D_{CO} around the 50% target. When $D_{CO}>50\%$, *PO* stays low; otherwise, a pulse is generated. The C_{RGL} and C_{RGR} are reset by a short pulse, S_{CV}, at the end of each *CO* period. When *PO* stays low, meaning that D_{CO} exceeds 50% (or V_{REC} exceeds V_{MPP}), a DC-DC enable signal, *COM*, is generated to start the DC-DC conversion. The lower hysteresis threshold, V_{RECS}, is generated by a switched-capacitor voltage divider. In this design, V_{RECS} can be turned from 97%×V_{REC} to 99.5%×V_{REC} to adjust the ripple of V_{REC} during DC-DC conversion.

The proposed circuit was fabricated in a 0.18µm BCD process and has an active area of 0.47mm^2 (Fig. 30.3.7). It is tested with a commercial PT (PEH-S128-H5FR-1107YB) excited at its resonance frequency of 230Hz. Figure 30.3.4 shows the measured waveform. The system starts from the cold state with V_{OC}=1.5V and L_M=27µH. V_{REC} then increases steadily because D_{CO} is less than 50% and the DC-DC converter is disabled. When V_{REC} reaches V_{MPP1} (~2.47V), D_{CO} is 50%, indicating that the MPP has been reached. The DC-DC converter is then enabled by the MPPT controller to maintain V_{REC} at 2.47V by transferring the harvested energy to V_S during the MPPT$_1$ period. When the vibration excitation is increased to V_{OC}=2V, the new V_{MPP} increases and D_{CO} becomes lower than 50%. The proposed circuit can sense the acceleration variation in half cycle and start to converge to the new MPP. As a result, the MPPT block disables the DC-DC converter so that V_{REC} builds up. After D_{CO} reaches 50% again, V_{REC} is maintained at the new MPP (~3.42V) in the MPPT$_2$ period. The MPPT convergence time is mainly affected by the capacitance of C_{REC}. The bottom-right plot shows the measured output power versus V_{REC} with the same V_{OC} and L_M as used in the waveform. It shows that the optimal V_{MPP} for 1.5V V_{OC} (or 2V V_{OC}) is 2.4V (or 3.3V), which is very close to the regulated V_{REC} of 2.47V (or 3.42V) measured and shown in the waveform. The zoomed-in V_{REC} waveform is also shown in the figure. Each regulation process is done through a number of DC-DC conversion cycles indicated by the pulse signal S_{PC}.

The output power of an SSHI rectifier versus the D_{CO} with 1.5V and 2V V_{OC} is shown in Fig. 30.3.5 (top-left). At their peak power points, the optimal duty cycles are 47.58% and 48.52% respectively, which are close to 50%. These results validate the analytical expression of η_{MPPT}. The shift of optimal D_{CO} from 50% to a slightly lower value is mainly due to the non-zero voltage drop of the active rectifier. However, thanks to the high tolerance to D_{CO} errors of the proposed MPPT algorithm, even when the system regulates D_{CO} to 50% instead of to the actual optimal value, the MPPT efficiency η_{MPPT} is maintained above 99%. The measured output power from an FBR and the proposed SSHI rectifier with different inductors (different η_F) at V_{OC}=2V shows that the proposed rectifier achieves a peak output power of 272.5µW, with 738% enhancement compared to an FBR (36.9µW). The MPPT efficiency with different input V_{OC} and η_F is also shown in Fig. 30.3.5 (bottom). From these two plots, regardless of V_{OC} and η_F, the optimal D_{CO} is always around 50%, while the η_{MPPT} remains high. The peak η_{MPPT} is 98% and the average efficiency is around 96% for a wide range of V_{OC} and η_F.

Fig. 30.3.6 compares the proposed MPPT design with the state-of-the-art. It occupies a compact area, while enabling continuous MPPT without using an explicit power sensor. It shows no dependency on rectifier parameters: V_{OC} and η_F. It achieves 98% peak MPPT efficiency and up to 738% power extraction enhancement compared to an FBR.

References:

[1] S. Li et al., "A Piezoelectric Energy-Harvesting System with Parallel-SSHI Rectifier and Integrated MPPT Achieving 417% Energy-Extraction Improvement and 97% Tracking Efficiency," *IEEE Symp. VLSI Circuits*, pp. C324–C325, June 2019.

[2] A. Morel, et al., "Self-Tunable Phase-Shifted SECE Piezoelectric Energy-Harvesting IC with a 30nW MPPT Achieving 446% Energy-Bandwidth Improvement and 94% Efficiency," *ISSCC*, pp. 488–489, Feb. 2020.

[3] M. Shim et al., "Self-powered 30µW-to-10mW Piezoelectric energy-harvesting system with 9.09ms/V maximum power point tracking time," *ISSCC*, pp. 406–407, Feb. 2014.

[4] D. A. Sanchez et al., "A 4µW-to-1mW Parallel-SSHI Rectifier for Piezoelectric Energy Harvesting of Periodic and Shock Excitations with Inductor Sharing, Cold Start-Up and Up to 681% Power Extraction Improvement," *ISSCC*, pp. 366–367, Feb. 2016.

[5] Z. Chen et al., "A Piezoelectric Energy-Harvesting Interface Using Split-Phase Flipping-Capacitor Rectifier and Capacitor Reuse Multiple-VCR SC DC-DC Achieving 9.3× Energy-Extraction Improvement," *ISSCC*, pp. 424–425, Feb. 2019.

[6] S. Li et al., "A 32nA Fully Autonomous Multi-Input Single-Inductor Multi-Output Energy-Harvesting and Power-Management Platform with 1.2×105 Dynamic Range, Integrated MPPT, and Multi-Modal Cold Start-Up," *ISSCC*, pp. 472–473, Feb. 2022.

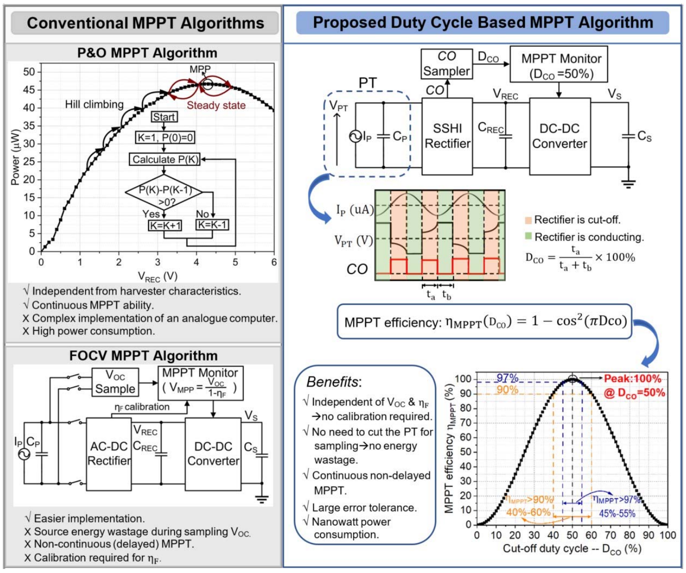

Figure 30.3.1: Conventional MPPT algorithms (left); simplified architecture, function and its graph of the proposed duty cycle based MPPT algorithm (right).

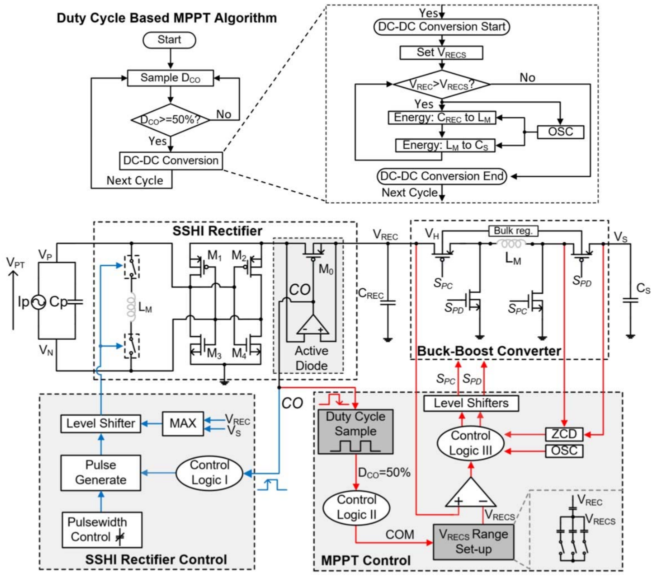

Figure 30.3.2: Duty cycle based MPPT algorithm and DC-DC working logic flow charts (top); block diagram of the proposed PEH system (bottom).

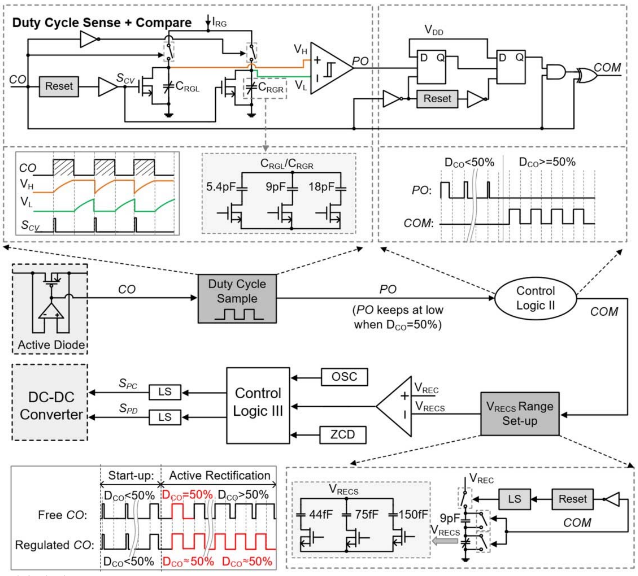

Figure 30.3.3: Duty cycle sampling block of the proposed system; output waveform of free CO without MPPT and regulated CO with proposed duty cycle controlling.

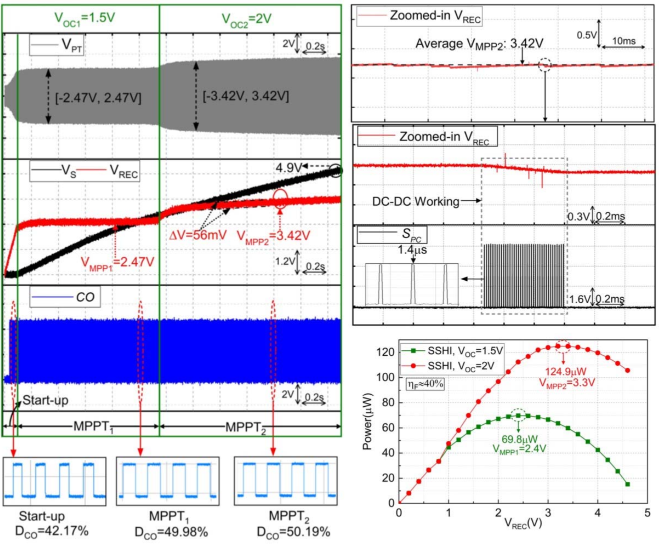

Figure 30.3.4: Measured waveforms of the MPPT transient time with input 1.5-V V_{OC} and 2-V V_{OC} (left); zoomed-in DC-DC converter working moment (top, right); measured output power of SSHI versus V_{REC} rectifier with 1.5-V and 2-V V_{OC} (bottom, right).

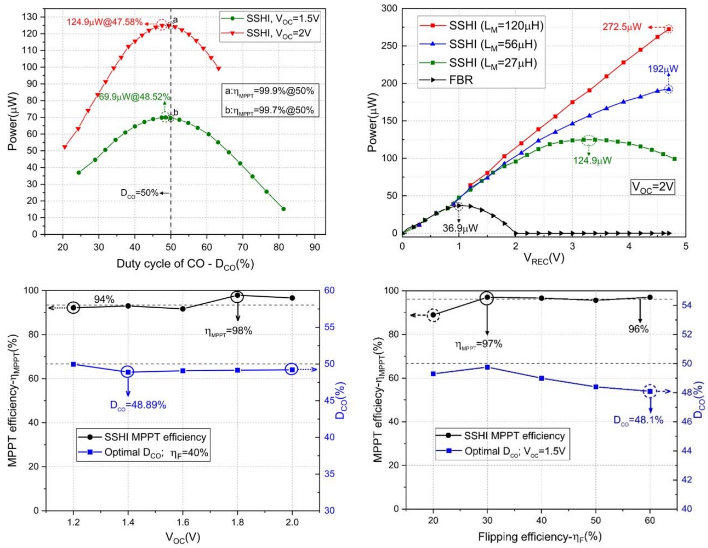

Figure 30.3.5: The measured output power versus D_{CO} (top, left); measured output power of proposed SSHI rectifier versus V_{REC} (top, right); MPPT efficiency and optimal D_{CO} versus different V_{OC} (bottom, left) and η_F (bottom, right).

	[3] ISSCC'14	[4]ISSCC'16	[5] ISSCC'19	[1] VLSI'19	[2] ISSCC'20	[6] ISSCC'22	**This work**
Technology (μm)	0.35	0.35	0.18	0.13	0.6	0.065	**0.18**
Technique	Comparator-based dual mode	P-SSHI	SPFCR	P-SSHI	PSECE	SECE	**SSHI**
Harvester Type	PEH-MIDE V21BL	PEH MIDE V21B & V22B	PEH-MIDE PPA1021	PEH-MIDE PPA1021 &PPA1011	PEH	TEG/PV/PEH	**PEH-S128-H5FR-1107YB**
Piezoelectric Capacitance(nF)	11	26, 20, 9	22	20 &100	24	24	**42**
Resonant Frequency(Hz)	100*	134.6-229.2	200	100-180	56	N/R**	**230**
MPPT Algorithm	FOCV	FOCV	FOCV	P&O	P&O	FOCV	**Duty Cycle Based**
Continuous MPPT	No	No	No	Yes	Yes	No	**Yes**
ADC/DCA, /Sensor Required	N/R**	N/R**	Yes	No	Yes	Yes	**No**
VOC Sampling Required	Yes	Yes	Yes	No	Yes	Yes	**No**
Peak MPPT Efficiency	99%	N/R**	N/R**	97%	94%	80%	**98%**
Quiescent Current (μA)	3	N/R**	N/R**	0.9	0.3	N/R**	**0.17**
Dimension (mm^2)	5.5	1.3*	0.21	1.07	14	3.11	**0.47**
P_{IC}/P_{FBR}@η_F	1X*@No	4.4X@89%/94%	6.5X-9.3X@89%	4.17X@86%	3.28X@No	3.2X@No	**7.38X@82%**

*Estimated from the paper
**N/R: not reported

Figure 30.3.6: Comparison table of proposed duty cycle based MPPT and state-of-the-art MPPT techniques.

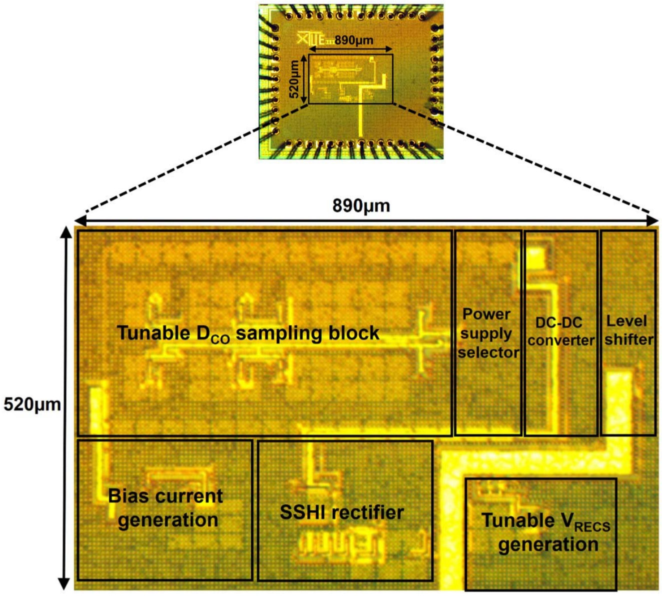

Figure 30.3.7: Die micrograph.